LAWRENCE
LIVERMORE
NATIONAL
LABORATORY

LLNL-JRNL-416351

Dense Plasma X-ray Scattering: Methods and Applications

S. H. Glenzer, H. J. Lee, P. Davis, T. Doppner, R. W. Falcone, C. Fortmann, B. A. Hammel, A. L. Kritcher, O. L. Landen, R. W. Lee, D. H. Munro, R. Redmer, S. Weber

August 31, 2009

High Energy Density Physics

Disclaimer

Dense Plasma X-ray Scattering: Methods and Applications

S.H. Glenzer[a], H. J. Lee[b], P. Davis[b], T. Döppner[a], R. W. Falcone[b], C. Fortmann[c], B. A. Hammel[a], A. L. Kritcher[b], O. L. Landen[a], R. W. Lee[a], D. H. Munro[a], R. Redmer[c], S. Weber[a]

[a] *L-399, Lawrence Livermore National Laboratory, University of California, P.O. Box 808, Livermore, CA 94551, USA*
[b] *Department of Physics, University of California, Berkeley, CA 94720, USA*
[c] *Institut für Physik, Universität Rostock, Universitätsplatz 3, 18051 Rostock, Germany*

Abstract

We have developed accurate x-ray scattering techniques to measure the physical properties of dense plasmas. Temperature and density are inferred from inelastic x-ray scattering data whose interpretation is model-independent for low to moderately coupled systems. Specifically, the spectral shape of the non-collective Compton scattering spectrum directly reflects the electron velocity distribution. In partially Fermi degenerate systems that have been investigated experimentally in laser shock-compressed beryllium, the Compton scattering spectrum provides the Fermi energy and hence the electron density. We show that forward scattering spectra that observe collective plasmon oscillations yield densities in agreement with Compton scattering. In addition, electron temperatures inferred from the dispersion of the plasmon feature are consistent with the ion temperature sensitive elastic scattering feature. Hence, theoretical models of the static ion-ion structure factor and consequently the equation of state of dense matter can be directly tested.

Key words: warm dense matter, plasma diagnostic, Thomson scattering, plasmons
PACS: 52.25.Os, 52.35.Fp, 71.45.Gm, 71.10.Ca

1. Introduction

Accurate characterization of dense and compressed matter with inelastic x-ray Thomson scattering is important for inertial confinement fusion and laboratory astrophysics experiments [1, 2]. In particular, the capability to measure electron temperature and density in dense plasmas allows testing of hydrodynamic modeling and of calculations of physical properties of dense matter. Present experiments are aimed towards the study of the physics of planetary formation [3] and composition [4, 5], as well as towards determining the equation of state (EOS) of light elements [6, 7, 8, 9]. One future challenge is the application of this technique to characterize compressed matter such as those produced on the National Ignition Facility where, e.g., hydrogen and beryllium will approach extremely dense states of matter of up to 1000 g/cc. In this regime, the density, compressibility, and the ratio of electron temperature to Fermi energy, can be directly measured from the Compton scattered spectrum of a high-energy x-ray line source. At lower densities, collective scattering on plasmons can be applied for the study of the assembly of thermonuclear fuel. Moreover, measurements of compressibility and conductivity employing plasmon scattering can provide important experimental data on physical quantities needed to model dense plasmas.

For applications in this field, we have developed x-ray Thomson scattering on the Omega laser facility. Experiments have employed isochorically heated solids [10, 11] and laser shock-compressed foils [12, 13] to access matter at solid density and above with electron densities approaching $n_e = 10^{24}\mathrm{cm}^{-3}$. Besides demonstrating the diagnostic capability for future spherical implosion studies, present experiments address fundamental physics questions by determining structure factors in two-component plasmas and the equation of state in dense matter. In addition, collective plasmon scattering measurements have been developed to provide measurements of collisions, quantum effects and thermodynamic equilibrium of dense matter [2].

In this study, we show that simultaneous Compton and plasmon scattering measurements from laser-irradiated foils accurately characterize dense compressed states of matter. These x-ray Thomson scattering experiments employ powerful laser-produced x-ray sources that penetrate through dense and compressed

Email address: glenzer1@llnl.gov (S.H. Glenzer)

materials with densities of solid and above. Here, we demonstrate that 6.2 keV He-alpha radiation from nanosecond laser plasmas fulfills the stringent requirements on photon numbers and bandwidth for spectrally-resolved x-ray Thomson scattering measurements from compressed beryllium in single shot experiments. We present experiments that have been performed in the non-collective and collective scattering regime, i,.e., in backward and forward scattering geometry, respectively.

In the Compton (backward) scattering regime, the scattering process is non coherent and the spectrum shows the Compton down-shifted line that is broadened by the thermal motion of the electrons [10]. In degenerate systems, the width of the Compton scattering line is thus determined by the Fermi energy providing a measurement of the electron density [13]. On the other hand, in non-degenerate heated matter the electron velocity distribution function transitions to a Maxwell-Boltzmann distribution and yields the electron temperature [14]. In this case, corrections due to the Pauli exclusion principle and finite collective effects must be included Thus, for the full interpretation of the elastic and inelastic scattering components from dense plasmas, the theoretical form factor of Chihara [15, 16] has been further developed by Gregori *et al* [17, 18, 19] to account for these effects and to include free-free and bound-free processes.

In the plasmon (forward) scattering regime, the collective plasmon feature has been observed at frequency shifts that are significantly smaller than that of the Compton scattering feature [11, 13]. In addition, at higher electron temperature, the up-shifted plasmon feature has been measured [20] that allows measurements of the temperature via the relation of detailed balance. The plasmon frequency shift is determined by the plasmon dispersion relation with the leading term being sensitive to the electron density while the electron temperature being a second order effect contributing to spatial propagation of plasmon (Langmuir) oscillations [21]. Importantly, in plasmas with accurately known density, the plasmon frequency thus provides estimates of the temperature. In addition, damping of the plasmon feature is an important observable in present experiments. The width of the plasmon is hence sensitive to temperature and collisions. In the latter case, theoretical approximations that use the Mermin approach to account for collisions [22] have provided consistent descriptions of experimental spectra [11].

The paper is organized as follows. In Section 2 we outline the theoretical basis for Thomson scattering in dense plasmas, introduce the dynamical structure factor as a central quantity for interpreting the scattering spectra. Results of these dynamic structure factor calculations are subsequently applied to the non-collective and collective Thomson scattering spectra from compressed matter. In Section 3, we describe these experiments, and in Section 4 we discuss experimental spectra and show sensitivity to the compressed matter conditions. In Section 5 we summarize and address future extensions of the x-ray scattering technique.

2. Theory

In this study, the plasma is irradiated by non-polarized x rays of energy E_0 and wavelength λ_0 from a laser-irradiated foil along the direction of the incident wave vector $\mathbf{k}_0$ with $k_0 = 2\pi/\lambda_0$. The detector observes the scattered radiation at the scattering angle θ in the direction of the scattered wave vector $\mathbf{k_S}$ at a distance much larger than the plasma extension. During the scattering process, the incident photon transfers, on average, momentum $\hbar\mathbf{k}$ and the Compton energy $E_C = \hbar\omega = \hbar^2k^2/2m_e = \hbar\omega_0 - \hbar\omega_1$ to the electron, where ω_1 is the frequency of the scattered radiation. In the non-relativistic limit ($\hbar\omega \ll \hbar\omega_0$) and for small momentum transfers we have $\mathbf{k} = 2\mathbf{k_0}\sin(\theta/2)$ and

$$k = |\mathbf{k}| = 4\pi\frac{E_0}{hc}\sin(\theta/2). \tag{1}$$

Equation (1) determines the scale length $\lambda^\star \approx 2\pi/k$ of the electron density fluctuations measured in the scattering experiment. The comparison with the screening length, λ_S determines the scattering regime. The dimensionless scattering parameter α

$$\alpha = \frac{1}{k\lambda_S} \tag{2}$$

is used. The screening length may be calculated numerically using Fermi integrals [2]or analytically using an effective temperature [17, 23]. In the non-degenerate case, with $\Theta = \frac{k_BT_e}{\epsilon_F} \gg 1$, with k_B being the Boltzmann constant, ϵ_F the Fermi energy, and T_e the electron temperature, we obtain the usual Debye screening length

$$\lambda_S^{-1} \rightarrow \lambda_D^{-1} = \left(\frac{n_e e^2}{\varepsilon_0 k_B T_e}\right)^{1/2}. \tag{3}$$

For degenerate systems ($\Theta \leq 1$), we obtain the Thomas-Fermi screening length.

$$\lambda_S^{-1} \rightarrow \lambda_{TF}^{-1} = \sqrt{\frac{m_e e^2}{\pi\varepsilon_0\hbar^2}\left(\frac{3n_e}{\pi}\right)^{1/3}}. \tag{4}$$

As seen from Eqs. (3, 4), λ_S is determined by the plasma conditions, density and temperature, while $\lambda^\star$ is primarily determined by the x-ray probe energy and the scattering angle (i.e. by the setup of the scattering experiment, Eq. (1)). The latter statement is only approximately fulfilled. When appropriate, the well-known corrections to the length of the scattering vector for the finite frequency shift of the scattered radiation and due to the dispersion of the radiation in the dense plasma need to be included. The scattering parameter defines the regime of a scattering experiment with $\alpha > 1$ indicating the collective scattering regime where collective plasmon and acoustic oscillations are observed. On the other, hand, for $\alpha << 1$ the scattering spectrum reflects the non-collective motion of the electrons.

With the scattering vector $\mathbf{k}$ defined by Eq. (1), the scattered power P_S from N electrons into a frequency interval $d\omega$ and solid angle $d\Omega$, i.e., the scattering spectrum [24], is determined by

$$P_S(\mathbf{R},\omega)d\Omega d\omega = \frac{P_0 r_0^2 d\Omega}{2\pi A} N S(\mathbf{k},\omega)d\omega. \times \left|\widehat{\mathbf{k}_S}\times(\widehat{\mathbf{k}_S}\times\widehat{\mathbf{E}}_0)\right|^2 . \quad (5)$$

In Eq. (5), P_0 denotes the incident x-ray power, A is the plasma area irradiated by the probe x-rays, and $S(\mathbf{k},\omega)$ the total electron dynamic structure factor. The polarization term reflects the dependence of the scattered power on the polarization of the incident radiation; for non polarized laser-produced x-ray sources, $|\widehat{\mathbf{k}_S}\times(\widehat{\mathbf{k}_S}\times\widehat{\mathbf{E}}_0)|^2 = (1-\frac{1}{2}\sin^2\theta) = \frac{1}{2}\left(1+\cos^2\theta\right)$.

By multiplying Eq. (5) with the length of the scattering volume, ℓ, it is seen that the scattered power depends on the setup of the scattering experiment (initial probe power, scattering angle, probe wavelength, probe polarization, detector solid angle), the electron density, the plasma length, and on the total dynamic structure factor $S(\mathbf{k},\omega)$. The structure factor is defined as the Fourier transform of the electron-electron density fluctuations, containing the details of the correlated many-particle system, cf. [26]. For non-collective scattering the random phase approximation [17, 25] that takes into account degeneracy, the Pauli exclusion principle, the Compton effect, and detailed balance is usually sufficient for calculating $S(\mathbf{k},\omega)$. For forward scattering experiments, the Born-Mermin (BM) approximation [22, 27] has been developed to include electron-ion collision effects on damping [11] and dispersion [21] of plasmons.

The full theoretical structure factor is applied throughout this study to infer plasma conditions from experimental spectra. However, simple analytical equations can be derived to illustrate the dependency of the scattering spectra on density and temperature. The frequency shift of a scattered photon by a free electron is determined by the Compton and the Doppler effects

$$\omega = -\hbar k^2/2m_e \pm \mathbf{kv} . \quad (6)$$

The former is due to the transfer of momentum from the incident photon to the electron during the scattering process resulting into the Compton downshift of the scattered radiation to lower x-ray energies. This term defines the inelastic scattering component in fully non-collective x-ray Thomson scattering experiments. Thus, the spectrum of the Compton-downshifted line reflects the velocity component of the electron in the direction of the scattering vector $\mathbf{k}$.

To calculate the number of electrons that contribute to the broadening via Eq. (6), the three-dimensional velocity space is considered. The number of electrons within the velocity interval v_x and $v_x + dv_x$ is proportional to the volume described by an annulus around v_x that must be integrated to include all possible projections of velocity vectors $\mathbf{v}$ onto v_x. With the Fermi distribution function applied for weakly degenerate plasmas, $k_B T_e < \epsilon_F$, where $v_F = (2\epsilon_F/m_e)^{1/2}$ is the Fermi velocity, [14] showed

$$f_0\left(\frac{v_x}{v_F}\right) \propto \int_0^{\pi/2} \frac{(v_x/v_F\cos\beta)^2\tan\beta d\beta}{e^{\left(\left(\frac{v_x}{v_F\cos\beta}\right)^2-\eta\right)/\left(\frac{T_e}{\epsilon_F}\right)}+1} , \quad (7)$$

with β being the angle between $\mathbf{v}$ and the v_x-axis and η is given by the Sommerfeld expansion

$$\eta = 1 - \left(\frac{\pi^2}{12}\right)\left(\frac{T_e}{\epsilon_F}\right)^2 . \quad (8)$$

The second term accounts for the fact that the chemical potential in the expression for the occupation of states for fermions, $(\exp(E-\mu)/k_B T_e+1)^{-1}$, has some temperature dependence at finite temperature. This expansion is valid for degenerate systems at finite temperature. The expression $\eta = (n_e\Lambda_e^3)/2$, where Λ_e is the thermal wavelength, is valid for nondegeneracy. A general solution is the inversion of Fermi integrals as mentioned after Eq. (2).

In a degenerate system, applying Eqs. (7-8) will provide the spectrum of the Compton line with the width proportional to $(\epsilon_F)^{1/2}$ and hence to $(n_e)^{1/3}$ providing the density of the plasma. In a non-degenerate plasma, on the other hand, the Compton scattering spectrum will reflect a Maxwell-Boltzmann distribution, and the width will yield a measurement of the electron temperature.

In addition to the Compton scattering component, elastic scattering at the incident x-ray energy as well as possible contributions of bound electrons to the inelastic scattering component will also need to be taken into account. The total electron dynamic structure factor $S(\mathbf{k},\omega)$ includes these effects for the full range of temperatures assessed in experiments and further accounts for finite values of α and quantum effects. It take the form

$$S_{ee}(k,\omega) = |f_I(k)+q(k)|^2 S_{ii}(k,\omega) + Z_f S^0_{ee}(k,\omega) + Z_b \int d\omega' \widetilde{S}_{ce}(k,\omega-\omega') S_S(k,\omega') \quad (9)$$

The first term in Eq. (9) accounts for the density correlations of electrons that dynamically follow the ion motion. This includes both the bound electrons, represented by the ion form factor $f_I(k)$, and the screening cloud of free (and valence) electrons that surround the ion, represented by $q(k)$. The ion-ion density correlation function, $S_{ii}(k,\omega)$, reflects the thermal motion of the ions and/or the ion plasma frequency. The second term in Eq. (9) gives the contribution to the scattering from the high frequency motion of the free electrons that do not follow the ion motion. Here, $S^0_{ee}(k,\omega)$ is the high frequency part of the electron-electron correlation function and it reduces to the usual electron feature in the case of an optical probe. The last term of Eq. (9) includes inelastic scattering by strongly bound core electrons, which arises from Raman transitions to the continuum of core electrons within an ion, $\tilde{S}_{ce}(k,\omega)$, modulated by the self-motion of the ions, represented by $S_s(k,\omega)$.

With decreasing scattering angle and with moderate x-ray probe energies, the scattering length increases and the scattering parameter assumes values with $\alpha > 1$. The scattering regime is collective and Eq. (9) will describe the collective electron plasmon oscillations and acoustic resonances. The latter are not resolved in present x-ray scattering experiments, and they are restricted to measure relative or absolute intensities of elastically scattered x rays [28, 29, 30]. On the other hand, the plasmon spectrum has been resolved with laser x-ray sources. The plasmon frequency shift from E_0 is determined by the plasmon dispersion relation and the width is determined by Landau damping and collisional damping processes. For small values of k using an inversion of Fermi integrals given by [31] that results in a modified analytical Bohm-Gross dispersion relation [21]

$$\omega^2_{pl} = \omega^2_p + 3k^2 v^2_{th}(1+0.088 n_e \Lambda^3_e) + \left(\frac{\hbar k^2}{2m_e}\right)^2 , \quad (10)$$

where $\omega_p = \sqrt{(n_e e^2/\varepsilon_0 m_e)}$ is the plasma frequency, $v_{th} = \sqrt{k_B T_e/m_e}$ is the thermal velocity and $\Lambda_e = h/\sqrt{2\pi m_e k_B T_e}$ is the thermal wave length.

In Eq. (10), the first term is a result of electron oscillations in the plasma [32], the second term represents the effect on propagation of the oscillation from thermal pressure. The third term includes degeneracy effects from Fermi pressure, and the last term is the quantum diffraction shift [33].

Independent of the evaluation of the dielectric function, the shape of the structure factor, and of modeling of collisional effects, the dielectric function fulfills the requirement,

$$\frac{S(\mathbf{k},\omega)}{S(-\mathbf{k},-\omega)} = \mathrm{e}^{-\hbar\omega/k_B T_e} . \quad (11)$$

This relation is referred to as detailed balance relation. As a general consequence, the structure factor shows an asymmetry with respect to $\mathbf{k}$ and ω. In the collective scattering regime and for conditions with sufficiently high temperatures, up-shifted plasmons have been observed to provide temperatures [20]. Temperatures achieved in the present study restrict plasmon measurements to the more intense red-shifted feature.

3. Compressed Matter Experiments

Figure 1 shows a schematic of the experiment that has been performed at the Omega laser facility [34]. Twelve laser beams smoothed with distributed phase plates (SG-4) overlap in ~ 1 mm diameter focal spot and directly illuminate a 250 μm thick beryllium foil, cf. Fig. 1(a). Each beam delivers up to about 480 J in a 1 ns square pulse. They are staggered in time with 3-4 ns long constant drive and laser intensities of $10^{14}\mathrm{Wcm}^{-2} < I < 10^{15}\mathrm{Wcm}^{-2}$.

In addition to the heater beams, twelve $1ns-$long probe beams, delayed in time, irradiate a 2μm thick Mn foil to produce $\mathrm{He}-\alpha$ x rays to probe the dense compressed plasma. In Fig. 1, the scattered probe x-rays have been observed in the downward direction employing a gated high efficiency crystal spectrometer [35, 36]. In this study, the detector provides four independent temporal gates of ~ 100 ps duration that are timed close to the end of the heater beams to avoid bremsstrahlung and to measure scattering spectra when the beryllium is homogeneously compressed.

Experiments have been performed in the Compton scattering regime with 90° and in the plasmon scattering regime with a 25° forward scattering angle. Figure 1(a)

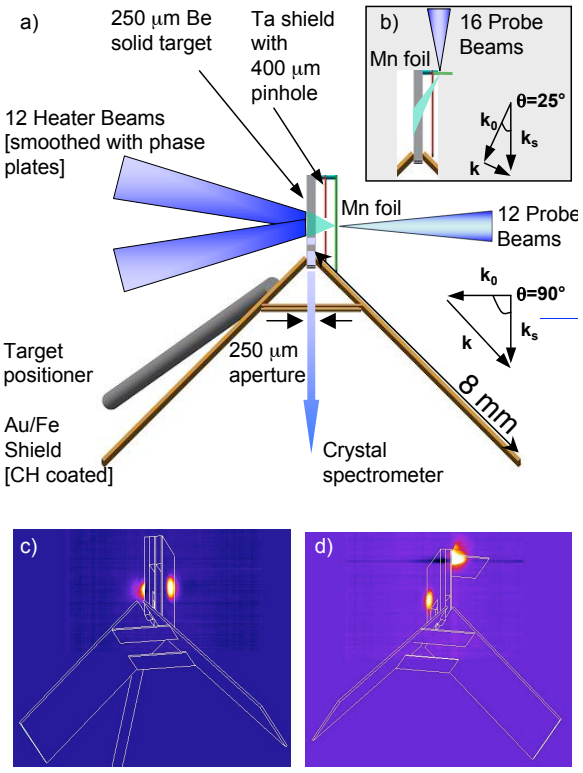

Figure 1: Schematic of the scattering experiment showing twelve heater beams that compress the Be foil and delayed probe beams that irradiate a Mn foil producing E = 6.2 keV He-alpha x-rays. X-ray scattering spectra are observed in the downward direction with a gated crystal spectrometer. (a) Experiments with a scattering angle of 90° employ 12 delayed probe beams while (b) a 25° forward scattering experiment is achieved with 16 probe beams. Time-integrated x-ray images for $E > 2$ keV show the emission produced by heater and probe beams for experiments with (c) 90° and (d) 25° scattering angle.

shows the **k**-vector diagram for the 90° scattering studies while Fig. 1(c) shows the high energy > 2 keV x-ray target emission from pinhole camera measurements that indicate the laser focal spot locations. For the 25° forward scattering experiment, Fig. 1(b) shows the **k**-vector diagram and Fig. 1(d) the x-ray pinhole camera measurements, respectively.

To accurately define the scattering angle and to avoid sampling a large spread of **k**-vectors, e.g., keeping $\Delta k/k < 0.2$ for 90° scattering, a Ta shield with a 400μm pinhole has been employed. The pinhole is placed in between the Be and Mn foils and thus restricts the solid angle of the x-ray probe to $d\Omega_{x-ray} \simeq \pi$ sr. The x-rays interact with a sample surface area matched to the area irradiated by the heater beams with $A \simeq 0.01$ cm^{-2} and a volume of $V \simeq 10^{-4}$ cm^3. The 8 mm-long Au/Fe shields

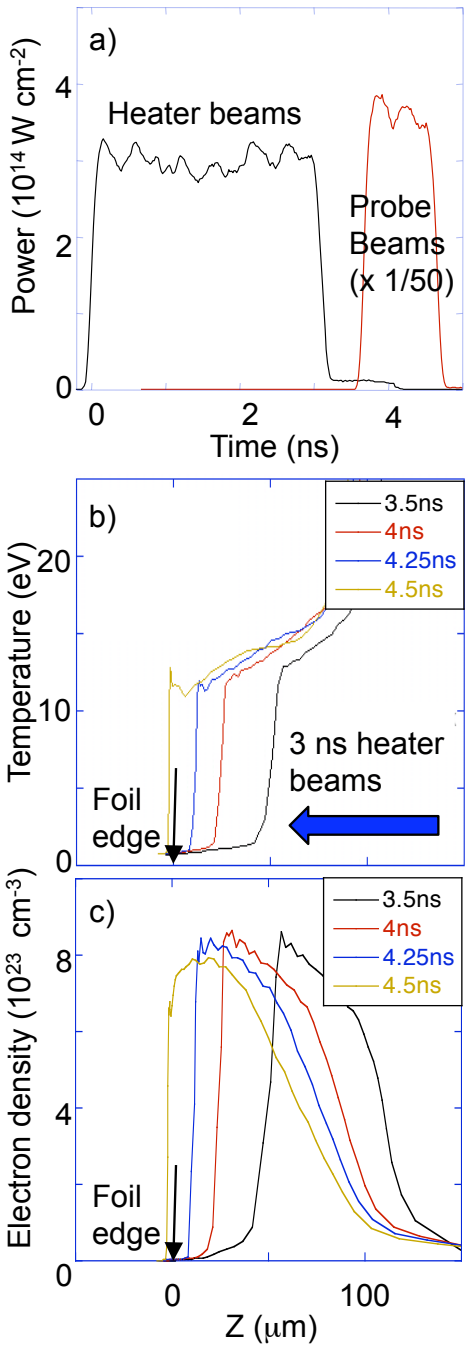

Figure 2: Laser pulses are shown for compressing solid-density beryllium and for producing Mn 6.2 keV probe x rays (a). The radition-hydrodynamic simulations at various times that use the code LASNEX show temperatures of order 13 eV in the dense shock-compressed region of the target while higher temperatures result in the low-density blow-off plasmas (b). Electron densities approach 8×10^{23}W cm^{-3} over a region of 80 μm indicating a factor of three compression (c).

restrict the field of view of the x-ray spectrometer to the beryllium sample and prevent the Mn plasma from moving into the field of view at the time when the scattering spectrum is measured.

A typical laser to He$-\alpha$ x-ray conversion efficiency of 5×10^{-3} into a bandwidth of $\Delta E/E = 0.5\%$ results in a total photon number of 5×10^{12} photons per incident laser energy in joules and into a solid angle of 4π sr. Here, laser pulses with averaged energies of 1 kJ per 100 ps have been applied in a geometry where the probe x-rays will interact with the dense plasma subtending a solid angle of $d\Omega \simeq \pi$ sr. This yields a peak x-ray brilliance of $B(6.2\ \mathrm{keV}) = 5 \times 10^{12}$ photons $\times 10^3 \times \pi/4\pi \simeq 10^{15}$ photons/100 ps/0.5% bw/sr at the dense plasma in a single shot.

Estimating attenuation of the probe x-rays in the dense plasma of $1/e$, a crystal spectrometer collection efficiency of 0.1 rad $\times$ 3 mrad$/4\pi \simeq 3 \times 10^{-5}$, and a detection efficiency for a gated microchannelplate detector and filter of $\simeq 0.01$, we obtain a collection fraction of 10^{-7}. For electron densities of $n_e = 7.5 \times 10^{23}$ cm^{-3}, the Thomson scattering cross-section of $\sigma_{Th} = \frac{8\pi}{3} r_0^2 = 0.665 \times 10^{-24}$ cm^2, and a path length of $\ell = 0.08$ cm, the scattering fraction is $n_e \sigma \ell = 0.04$. Combining the peak brightness with the scattering fraction and collection efficiency, the total number of collected photons is 3×10^6 from which we can estimate a signal to noise ratio of about 100.

Figure 2 shows the laser intensity and radiation-hydrodynamic calculations of the experiment. The results indicate that the irradiation conditions employed in this study launch a strong shock wave into the solid beryllium compressing the target by a factor of three at pressures in the range of 20-35 Mbar. At $t = 4.5$ ns, when the shock has traversed the 250 μm thick foil, the twelve delayed probe beams produce Mn He-alpha radiation to scatter on the dense plasma. The calculations indicate that for $I = 3 \times 10^{14}$ W cm^{-2} the target is compressed by a factor of 3 with fairly homogeneous electron density profiles with 7×10^{23} cm^{-3} $< n_e <$ 8×10^{23} cm^{-3} and temperatures of 12eV $< T <$ 14 eV in the dense beryllium. Au/Fe shields collimate the field of view of the x-ray spectrometer avoiding detection of scattered light from the coronal plasma and further reduces background due to bremsstrahlung emission.

4. Thomson Scattering Results from compressed Matter

Figure 3 shows 90° scattering spectra from compressed beryllium. In contrast to x-ray scattering measurements on isochorically heated beryllium [10], a high-energy x-ray source with incident energy of $E_0 >$ 6 keV had been required to penetrate through compressed matter that is approaching $n_e = 10^{24}$ cm^{-3}. Although of sufficient x-ray energy, the present source has the disadvantage of consisting of two spectral features comprised of the 6.18 keV Mn He$-\alpha$ line and the 6.15 keV intercombination line with approximately equal intensity [38], cf. Fig. 5(a).

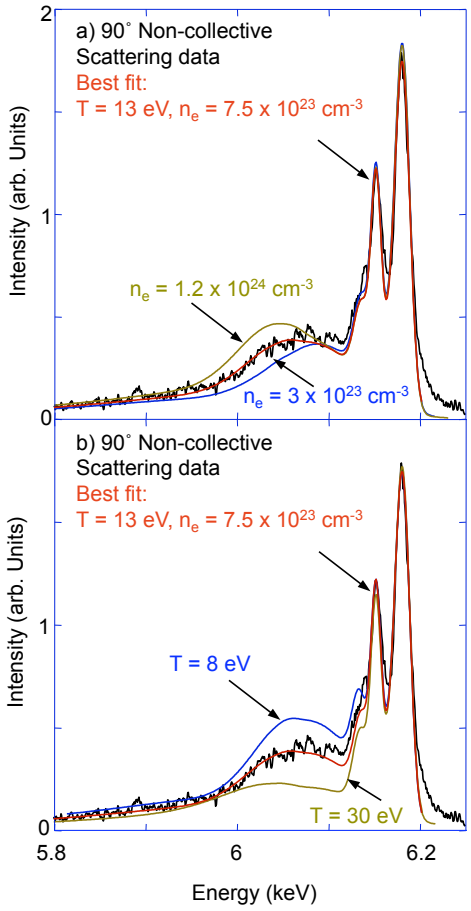

Figure 3: (a) X-ray scattering data for 90° scattering angle are shown along with theoretical spectra for various electron densities. (b) Same as in (a) for various ion temperatures.

Both features contribute to the Compton scattering spectrum that shows a parabolic spectrum downshifted in energy from the incident radiation by the Compton effect; the shift is determined by the Compton energy $E_C = \hbar^2 k^2/2m_e = 74$ eV. Here, the scattering vector is $k = 4.4$Å^{-1} indicating non-collective scattering with a scattering parameter $\alpha = 1/k\lambda_S = 0.5$. The Compton scattering spectrum directly reflects the electron distribution function; for a Fermi-degenerate system the

width of the Compton spectrum yields the Fermi energy,

$$E_F = \frac{\hbar^2}{2m_e}(3\pi^2 n_e)^{2/3} \ . \quad (12)$$

The fit of the experimental data using the theoretical form factor, Eq. (9), shows that the width of the Compton feature is sensitive to the electron density. The electron feature is derived with the Random Phase Approximation and the ion feature is fitted consistently with results from calculations using density-functional theory [29, 39]. The fit takes into account the detailed spectral features of the Mn source spectrum as well as instrument broadening. In addition, the small level of continuum radiation observed after the end of the heater pulse has been subtracted and corrections due to the spectral response of the spectrometer have been included.

Figure 3(a) compares the data to calculations with varying electron density ranging from non-compressed Be with $n_e = 3 \times 10^{23}\mathrm{cm}^{-3}$ to more than four-fold compression with $n_e = 1.2 \times 10^{24}\mathrm{cm}^{-3}$. Due to the small noise levels, the data determine the electron density to be $n_e = 7.5 \times 10^{23}\mathrm{cm}^{-3}$ with the corresponding Fermi energy of $E_F = 30$ eV with an error bar of ± 7 % in electron density.

Relating the Fermi energy with the electron density via Eq. (12) is motivated by the distribution function inferred from fitting the experimental Compton scattering data. Bound-free transitions have been included using hydrogenic wave functions. This contribution results in a small increase of the width of the inelastic scattering feature; the latter is dominated by the contribution from free electrons. The main effect is a high energy tail with shifts > 100 eV as apparent in the data and in the fits. The ionization state has been set to $Z = 2$ in agreement with previous experiments on isochorically heated beryllium at the same temperature and with radiation-hydrodynamic modeling. The shape of the Compton feature in Fig. 3 is consistent with this value with an estimated accuracy of ± 25 %; the latter takes into account the fact that the density from plasmons agrees with the Compton scattering data.

The intensity of the elastic scattering feature indicates a temperature significantly lower than the Fermi energy. In the present conditions with large scattering vector, the contribution from electrons in the screening cloud is negligible, and the strength of the elastic scattering feature is approaching $f^2 S_{ii}(k,\omega)$ [16, 40]. The ion form factor $f(k)$ is a measure of the number of bound electrons and $S_{ii}(k,\omega)$ is the ion-ion density correlation function. Thus, with absolute calibration provided by the measured strength of the inelastic Compton scattering feature and knowledge of the electron density, $S_{ii}(k,\omega)$ is determined absolutely from the experimental scattering data. Consequently, the ion temperature can be inferred from the intensity ratio of elastic to inelastic scattering.

Figure 3(b) indicates that this procedure is sensitive to variations in temperature leading to error bars in the temperature of 10 % for conditions with well-known structure factors. For the k-vector of Fig. 3(b), we employ the previously tested theory of Refs. [17, 19, 29] leading to a temperature of $T = 13$ eV. These scattering spectra show a significant difference from cold beryllium as shown in, e.g., Ref. [10] further indicating sensitivity to density and temperature.

Figure. 4 shows a comparison of the experimental data with theoretical spectra for different values of the ionization state, Z. In addition, the bound-free contribution to the scattering spectra are shown as the shaded area for high energy shifts. This comparison shows the sensitivity of scattering data to ionization state variation. Red and blue lines are the best fits when choosing $Z_f = 2$ and $Z_f = 1.5$, respectively. The ionization state affects both the intensity and the shape of inelastic scattering spectra. Assuming a decrease of ionization state in a fixed electron density corresponds to an increase of ion density through the relation of $n_e = Z_f n_i$ thus an increase of the ratio of the elastic to inelastic scattering feature. The contribution from bound-free transitions is shaded showing an increase of bound-free transitions in the case of $Z_f = 1.5$, cf. last term of Eq. (9) and $Z_{total} = Z_f + Z_b$. Since the ion temperature is also affecting the relative intensity of inelastic to the elastic scattering features, we obtain the optimum values for the temperature and ionization state through the best fitting and rms differences between the fit and the data as shown in inset of Fig. 4. The dark blue island in the center provides $Z_f = 2$ with ± 15 % accuracy.

Figure. 5 shows plasmon scattering data from experiments accessing the collective scattering regime with $\alpha = 1.56$ and $k = 1.36\text{Å}^{-1}$. In contrast to non-collective scattering, the broad inelastic Compton scattering feature is replaced with two small plasmon features, that are shifted in energy by ∼ 40 eV from the incident x-ray probe features. Here, one plasmon scattering feature is observed shifted from both incident x-ray features (i.e., He-alpha and intercombination line). In this case, the frequency shift due to the Compton effect is small of order 7 eV and the frequency shift of the plasmon is determined by the frequency of plasma (Langmuir) oscillations.

In this study, the resolution of the forward scattering measurements do not allow to sensitively resolve collisional broadening and both the random phase approxi-

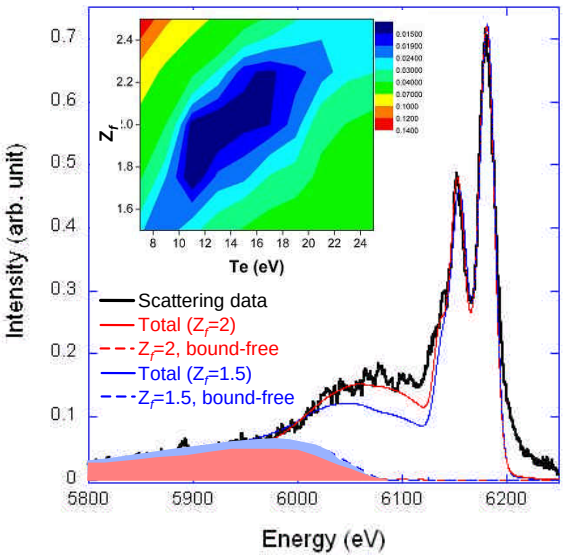

Figure 4: x-ray scattering data for 90° scattering angle are shown with ionization state variation in the theoretical spectra. Best fit with Z_f = 2 (red) is compared to fit with Z_f = 1.5 (blue). Here, T_e = 13 eV and $n_e = 7.5\times10^{23}\text{cm}^{-3}$. Inset shows the rms values between fits and data indicating the sensitivity to varying temperature and ionization state.

mation and the Born-Mermin collision theory fit the experimental data. Here, theoretical calculations convoluted with the incident Mn x-ray probe spectrum show the same plasmon shift and only small differences of the plasmon width. In addition, the experimental plasmon features are observed to be of significantly stronger intensity than elastically scattered dielectronic satellites associated with the Mn He-alpha resonance transition, cf. Fig. 5(a).

Figure 6 shows the experimental scattering data measured at 25° scattering angle together with theoretical calculations with various densities (a) and temperatures (b). The theoretical spectra yield the same densities and temperatures as obtained for non-collective scattering; comparing the scattering data with spectra calculated at various densities indicates that the frequency shift of the plasmon provides an accurate measure of the electron density of $n_e = 7.5\times10^{23}\text{cm}^{-3}$ with an error bar of ±6 %. Conversely, using the electron density from the 90° scattering data, we obtain an estimate of $T_e = 13 \pm 3$ eV for the electron temperature from the thermal corrections to the plasmon dispersion.

In shots at various laser intensities, we changed the shock properties, i.e. the density and the temperature. The resulting values for T and the Fermi energy according Eq. (12) are summarized in Fig. 7. The ex-

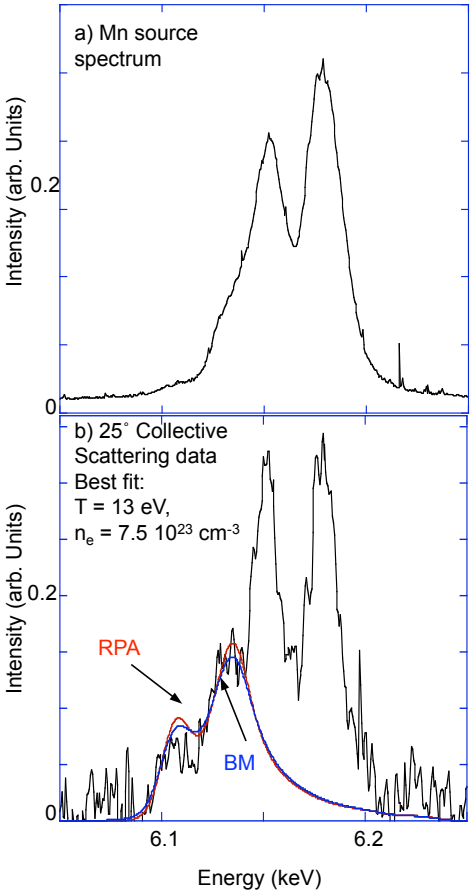

Figure 5: (a) The Mn x-ray probe spectrum is shown along with (b) x-ray scattering data for 25° scattering angle. Theoretical spectra of the inelastic plasmon scattering features are shown that use the random phase approximation and the Born-Mermin approximation indicating the same plasmon frequency shift and only small increase of the observable widths due to collisions.

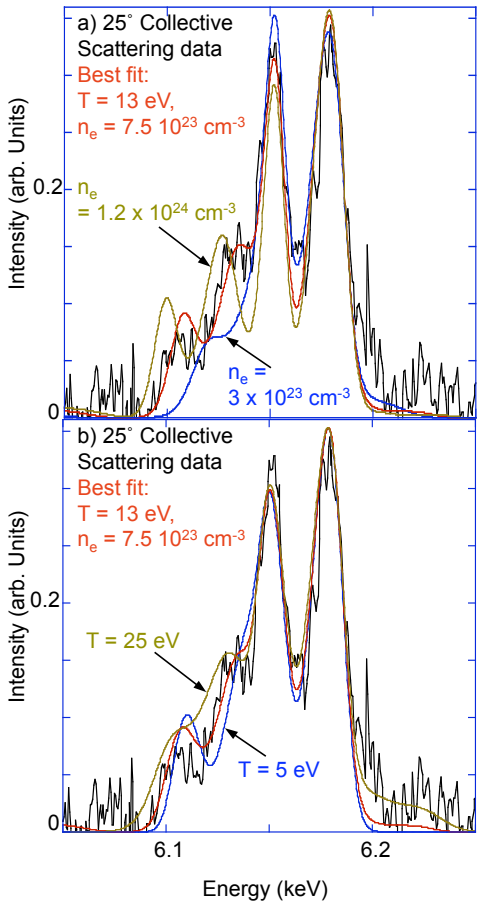

Figure 6: (a) X-ray scattering data for 25° scattering angle are shown along with theoretical spectra for various electron densities. (b) Same as in (a) for various electron temperatures.

periments demonstrate a direct measurement of the degeneracy and adiabat in these single-shocked foils. The direct comparison with LASNEX simulations that use the LEOS equation of state [41] show excellent agreement with the data. The simulations indicate slightly lower compression than the Hugoniot data predicted by LEOS by taking into account x-ray preheat and averaging over the densities in the shocked region, cf. Fig. 1(d). The agreement with LASNEX indicates that the conditions at low drive show observable effects of gradients. However, the data measured at higher drive agree well with both with LASNEX and LEOS.

Also, shown are calculations of the conditions predicted for ICF experiments during the implosion phase. These calculation use a beryllium ablator and predict ignition and gain employing a 1.2 MJ laser drive on the National Ignition Facility. The present experiment shows that these conditions are accessible by x-ray Thomson scattering that motivate a direct measurement of the degeneracy [42] during the assembly of the thermonuclear fuel.

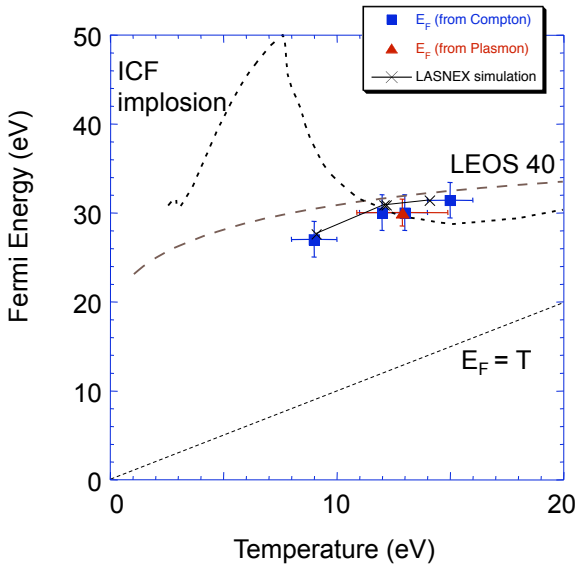

Figure 7: Fermi energies inferred from the measured densities from the Compton and plasmon scattering data are shown versus temperature. A high level of degeneracy is found close to predictions from LASNEX (solid curve) and the LEOS data table (long dashed). Also shown are the trajectory of beryllium in ICF implosion modeling (dashed) together with the curve $E_F = T$ (short dashed).

5. Summary

In summary, we have demonstrated collective and non-collective x-ray Thomson scattering techniques in

shock-compressed matter conditions. These measurements have provided accurate and mutually consistent data on density and temperature in close agreement with calculations. This method allows application to a number of dense matter questions including future applications to measure degeneracy and adiabat, e.g., in ICF and high energy density physics studies.

6. Acknowledgments

This work performed under the auspices of the U.S. Department of Energy by Lawrence Livermore National Laboratory under Contract DE-AC52-07NA27344. Also supported by the National Laboratory User Facility, Laboratory Directed Research and Development grants 08-ERI-002 and 08-LW-004, by the Helmholtz association (VH-VI-104), and by the Deutsche Forschungsgemeinschaft (SFB 652).

References

[1] J. D. Lindl *et al.*, Phys. Plasmas **11**, 339 (2004).
[2] S. H. Glenzer and R. Redmer, Rev. Mod. Phys. (2009), *in print*.
[3] H. C. Connolly, Jr., Stanley G. Love, Science **280**, 62 (1998).
[4] T. Guillot, Science **286**, 72 (1999).
[5] N. Nettelmann et al., Astrophys. J. 683, 1217 (2008).
[6] N. C. Holmes, M. Ross, W. J. Nellis, Phy. Rev. B. **52**, (1995).
[7] G. W. Collins et al., Science **281**, 1178 (1998).
[8] M. D. Knudson, D. L. Hanson, J. E. Bailey, C. A. Hall, J. R. Asay, Phys. Rev. Lett. **87** (2001).
[9] A. L. Kritcher *et al.*, Science, **322**, 69 (2008).
[10] S. H. Glenzer *et al.*, Phys. Rev. Lett. **90**, 175002 (2003).
[11] S. H. Glenzer *et al.*, Phys. Rev. Lett. **98**, 065002 (2007).
[12] H. Sawada *et al.*, Phys. Plasmas **14**, 122703 (2007).
[13] H. J. Lee *et al.*, Phys. Rev. Lett. **102**, 115001 (2009).
[14] O. L. Landen *et al.*, J. Quant. Spectr. Rad. Trans. **71**, 465 (2001).
[15] J. Chihara, J. Phys. F **17**, 295 (1987).
[16] J. Chihara, J. Phys.: Condens. Matter, **12**, 231 (2000).
[17] G. Gregori, S. H. Glenzer, W. Rozmus, R. W. Lee, and O. L. Landen, Phys. Rev. E **67**, 026412 (2003).
[18] G. Gregori, S. H. Glenzer, and O. L. Landen, Phys. Rev. E **74**, 026402 (2006).
[19] G. Gregori, A. Ravasio, A. Hoell, S.H. Glenzer, and S. J. Rose, High Energy Den. Phys. **3**, 99 (2007).
[20] T. Döppner, O. L. Landen, H. J. Lee, P. Neumayer, S. P. Regan, S.H. Glenzer, High Energy Den. Phys. **3**, 99 (2009).
[21] R. Thiele *et al.* Phys. Rev. E **78**, 026411 (2008).
[22] R. Redmer *et al.*, IEEE Trans. Plasma Science **33**, 77 (2005).
[23] M. W. C. Dharma-wardana and F. Perrot, Phys. Rev. Lett. **84**, 959 (2000).
[24] J. Sheffield, *Plasma Scattering of Electromagnetic Radiation* (Academic Press INC., New York, 1975).
[25] D. Pines and D. Bohm, Phys. Rev. **85**, 338 (1952).
[26] S. Ichimaru *Statistical Plasma Physics* (Addison., New York, 1994).
[27] A. Höll *et al.*, Eur. Phys. J. D **29** 159 (2004).
[28] E. G. Saiz *et al.*, Nature Phys., **4**, 940 (2008).
[29] J. Vorberger *et al.*, Phys. Rev. Lett. (2009), *submitted*.
[30] A. L. Kritcher *et al.*, Phys. Rev. Lett. (2009), *submitted*.
[31] R. Zimmerman, *Many-Particle Theory of Highly Excited Semiconductors* (Teubner, Leipzig, 1987).
[32] L. Tonks and I. Langmuir, Phys. Rev. **33**, 195 (1929).
[33] F. Haas *et al.*, Phys. Rev. E **62**, 2763 (2000).
[34] J. M. Soures *et al.*, Fusion Technology, **30**, 492 (1996).
[35] S. H. Glenzer *et al.*, Phys. Plasmas **10**, 2433 (2003).
[36] M.K. Urry *et al.*, J. Quant. Spectr. Trans. **99**, 636 (2006).
[37] G. B. Zimmerman and W. L. Kruer, Comments Plasma Physics and Controlled Fusion **2**, 51 (1975).
[38] D. B. Sinars *et al.*, Rev. Sci. Instrum. **77**, 10E309 (2006).
[39] K. Wünsch *et al.*, Phys. Rev. E **77**, 056404 (2008).
[40] D Riley, J J Angulo Gareta, A Benuzzi-Mounaix, M Esposito, E Garcia Saiz, C Gregory, F Y Khattak, M Koenig, M J Lamb, D McSherry, D Neely, M Notley, N Ozaki, M Rabec Le Gloahec, A Ravassio, K A Thornton and N C Woolsey, Plasma Phys. Control. Fusion **47**, 491 (2005).
[41] R. M. More *et al.*, Phys. Fluids **31**, 3059 (1988).
[42])A. L. Kritcher, P. Neumayer, M. Urry, H. Robey, C. Niemann, O. L. Landen, E. Morse, and S. H. Glenzer, High Energy Den. Phys. **3**, 156 (2007).